

# Carrier envelope phase and pulse shape effects on vacuum pair production in asymmetric electric fields with bell-shaped envelopes

Abhinav Jangir\* and Anees Ahmed†

*Department of Physics, MNIT Jaipur, Jaipur, Rajasthan, India*

(Dated: January 23, 2026)

We investigate the combined effects of carrier envelope phase and laser pulse shape on electron-positron pair production in the presence of an external time-dependent asymmetric electric field by solving the quantum Vlasov equation. We analyze how the pulse asymmetry, the envelope type (Gaussian, Lorentzian and Sauter), and the carrier envelope phase jointly influence the momentum distribution and the number density of created pairs. Our results show that pair production exhibits extreme sensitivity to both the degree of temporal asymmetry and the steepness of the envelope on either side of the pulse. These effects are qualitatively explained through a turning-point analysis, which, for the first time, is carried out for a non-analytic electric field using a regularization scheme. We observed that multiphoton pair production dominates the Schwinger mechanism in the case of a long falling-pulse asymmetry. For a short falling pulse with a flat-topped profile, pair production is further facilitated. We demonstrate that the number density can be enhanced by two to three orders of magnitude by choosing certain field parameters.

## I. INTRODUCTION

Dirac's prediction of the positron [1] paved the way for Sauter to demonstrate that the vacuum can decay into electron-positron pairs in the presence of a very strong static electric field [2]. Later, in 1951, Schwinger derived the pair production rate in a constant electric field using the proper-time method [3], identifying the critical field strength  $E_{\text{cr}} = m^2 c^3 / e\hbar \approx 1.3 \times 10^{18} \text{ V/m}$  as the threshold for producing observable pairs, where  $m$  and  $e$  are the electron mass and fundamental charge respectively. The field strength  $E_{\text{cr}}$  corresponds to a laser intensity  $\sim 10^{29} \text{ W/cm}^2$ , far exceeding present laser capabilities. Although chirped-pulse amplification (CPA) [4] technology has dramatically increased achievable laser intensities, researchers at CoReLS demonstrated a record-high peak laser intensity exceeding  $10^{23} \text{ W/cm}^2$  [5] by tightly focusing a petawatt-class laser pulse. This is still far beyond the critical laser intensity. Consequently, direct experimental verification of the Schwinger effect is still pending. The advent of the Extreme Light Infrastructure (ELI) [6], the X-ray free electron laser (XFEL) [7, 8] and eXwatt Center of Extreme Light Studies (XCELS) [9] may enable experimental investigations of QED vacuum decay into electron-positron pairs in the near future.

The non-perturbative non-equilibrium process of electron-positron pair production has been studied using a variety of approaches, including the WKB approximation [10], effective Lagrangian techniques [11], worldline instanton methods [12], the Wigner formalism [13–17], and the quantum Vlasov equation (QVE) [18–21]. Although all of these approaches provide the pair production rate, the QVE has the advantage of yielding the momentum distribution of the produced pairs. Being fully

non-perturbative, the QVE naturally incorporates contributions from both multiphoton absorption (a perturbative effect [22–24]) and the Schwinger effect (a purely non-perturbative effect which can be interpreted as a tunneling phenomenon).

Numerous studies have explored the influence of various field configurations on pair production. The impact of the laser frequency, carrier phase and pulse length on momentum distribution was studied for a short-pulse laser with subcycle structure in [25]. Other work has focused on the dynamically assisted Schwinger mechanism, which can significantly enhance the pair production rate [26–29]. Frequency chirping has been studied as another means to enhance the pair production rate [13, 30–32]. It has also been observed that the temporal asymmetry in the electric field can enhance the particle density by a few orders of magnitude [14, 33, 34].

In this work, we study the combined effects of the carrier-envelope phase and laser pulse shape on electron-positron pair production in the presence of a time-dependent asymmetric external electric field. We numerically solve the QVE for three different bell-shaped envelopes. These envelopes are related to the Gaussian, Sauter-type and Lorentzian functions, and are defined to have a range of properties such as fast versus slow decay, flat-topped versus peaked. This approach allows us to present results that are broadly applicable to generic bell-shaped pulses.

Our analysis shows that both the momentum distribution and the number density of produced pairs are highly sensitive to the carrier-envelope phase, pulse asymmetry and pulse shape. Using a semiclassical treatment based on the turning points of the potential (of the equivalent 1D scattering problem) in the complex-time plane, we confirm that the interference patterns in the momentum distribution arise from the interaction between these turning points. We also discuss how the number density can be enhanced by a suitable choice of the field parameters. Most plots in this work show results for

\* 2022rpy9087@mnit.ac.in

† anees.phy@mnit.ac.in

the Gaussian envelope, as the differences between the three envelopes are often qualitatively similar; when this is not true, we present plots for all three. Throughout this study, we use natural units ( $\hbar = c = 1$ ).

The paper is organized as follows: In Sec. II, we briefly review the QVE approach and introduce the external electric field. Sec. III presents numerical results for the momentum distribution, including a semiclassical analysis based on turning points. We discuss the number density in Sec. IV and conclude in Sec. V.

## II. THEORETICAL FORMALISM : THE QUANTUM VLASOV EQUATION

We consider a linearly polarized spatially homogeneous but time-dependent external electric field

$$\mathbf{E}(t) = E(t) \hat{z}. \quad (1)$$

The corresponding vector potential ( $A_0, \mathbf{A}$ ) may be chosen as

$$A_0 = 0, \quad \mathbf{A}(t) = A(t) \hat{z}, \quad A(t) = - \int_{-\infty}^t E(t') dt. \quad (2)$$

The details of the electric field are provided in Subsec. II A.

The central quantity that we study in this work is the distribution function  $f_{\mathbf{k}}(t)$ , which obeys an integro-differential equation called the quantum Vlasov equation given by

$$\begin{aligned} \frac{df_{\mathbf{k}}(t)}{dt} &= Q_{\mathbf{k}}(t) \int_{-\infty}^t dt' Q_{\mathbf{k}}(t') (1 - 2f_{\mathbf{k}}(t')) \\ &\quad \times \cos \left( 2 \int_{t'}^t dt'' \Omega_{\mathbf{k}}(t'') \right) \end{aligned} \quad (3)$$

where

$$Q_{\mathbf{k}}(t) = \frac{eE(t) \sqrt{m^2 + \mathbf{k}_{\perp}^2}}{2\Omega_{\mathbf{k}}^2(t)}, \quad (4)$$

$\mathbf{k} = (\mathbf{k}_{\perp}, k_z)$  is the canonical momentum and

$$\Omega_{\mathbf{k}}(t) = \sqrt{(k_z - eA(t))^2 + \mathbf{k}_{\perp}^2 + m^2} \quad (5)$$

is the instantaneous single-particle energy.

At asymptotic times ( $t \rightarrow \pm\infty$ ), when the external electric field is turned off, the distribution function acquires a clear particle interpretation:  $f_{\mathbf{k}}(\pm\infty)$  represents the density of pairs produced with momentum  $\mathbf{k}$ . At intermediate times, however, the field is non-zero and  $f_{\mathbf{k}}(t)$  contains contributions from both real and virtual excitations, so it does not admit a particle interpretation. A further requirement for such an interpretation is that the external electric field should vary slowly (adiabatic approximation) [18]. For these reasons, throughout this

work we restrict our analysis to the asymptotic distribution function

$$f_{\mathbf{k}}(\infty) = \lim_{t \rightarrow \infty} f_{\mathbf{k}}(t), \quad (6)$$

and the corresponding total number density

$$N = 2 \int \frac{d^3 \mathbf{k}}{(2\pi)^3} f_{\mathbf{k}}(\infty), \quad (7)$$

where the factor of 2 accounts for the electron spin degeneracy.

The integro-differential form of the quantum Vlasov equation (3) may be rewritten as a system of three coupled first-order ordinary differential equations [35]:

$$\begin{aligned} \frac{df_{\mathbf{k}}(t)}{dt} &= \frac{1}{2} Q_{\mathbf{k}}(t) g_{\mathbf{k}}(t), \\ \frac{dg_{\mathbf{k}}(t)}{dt} &= Q_{\mathbf{k}}(t) (1 - 2f_{\mathbf{k}}(t)) - 2\Omega_{\mathbf{k}}(t) h_{\mathbf{k}}(t), \\ \frac{dh_{\mathbf{k}}(t)}{dt} &= 2\Omega_{\mathbf{k}}(t) g_{\mathbf{k}}(t), \end{aligned} \quad (8)$$

This system defines an initial-value problem with  $f_{\mathbf{k}}(-\infty) = g_{\mathbf{k}}(-\infty) = h_{\mathbf{k}}(-\infty) = 0$ . This ODE formulation is significantly more convenient for numerical implementation than the original integro-differential equation (3).

### A. External electric field configuration

We consider time-dependent external electric fields of the form

$$E(t) = E_0 \cos(\omega t + \varphi) \left( \mathcal{E}(t; \tau_1, \nu) \Theta(-t) + \mathcal{E}(t; \tau_2, \nu) \Theta(t) \right) \quad (9)$$

where  $E_0$  is the amplitude,  $\Theta(t)$  is the Heaviside step function,  $\omega$  is the carrier frequency and  $\varphi$  is the carrier-envelope phase (CEP). The object  $\mathcal{E}(t; \tau, \nu)$  is a bell-shaped envelope centered at the origin, characterized by a width parameter  $\tau$  and a steepness parameter  $\nu$ . The electric field becomes asymmetric about  $t = 0$  whenever  $\tau_1 \neq \tau_2$  and, to quantify this asymmetry, we introduce the *pulse asymmetry parameter*  $\beta = \tau_2/\tau_1$ . The falling edge of the pulse is compressed for  $\beta < 1$  and elongated for  $\beta > 1$ . The order  $\nu$  controls the steepness of the envelope on either side of  $t = 0$ ; for a super-Gaussian envelope  $\nu$  is referred to as the *super-Gaussian order*.

In this work, we focus on the following envelopes:

$$\text{Gaussian: } \mathcal{E}(t; \tau, \nu) = \exp \left( -\frac{t^{2\nu}}{2\tau^{2\nu}} \right) \quad (10)$$

$$\text{Lorentzian: } \mathcal{E}(t; \tau, \nu) = \frac{1}{1 + (t/\tau)^{2\nu}} \quad (11)$$

$$\text{Sauter: } \mathcal{E}(t; \tau, \nu) = \operatorname{sech}^{2\nu} \left( \frac{t}{\tau} \right) \quad (12)$$

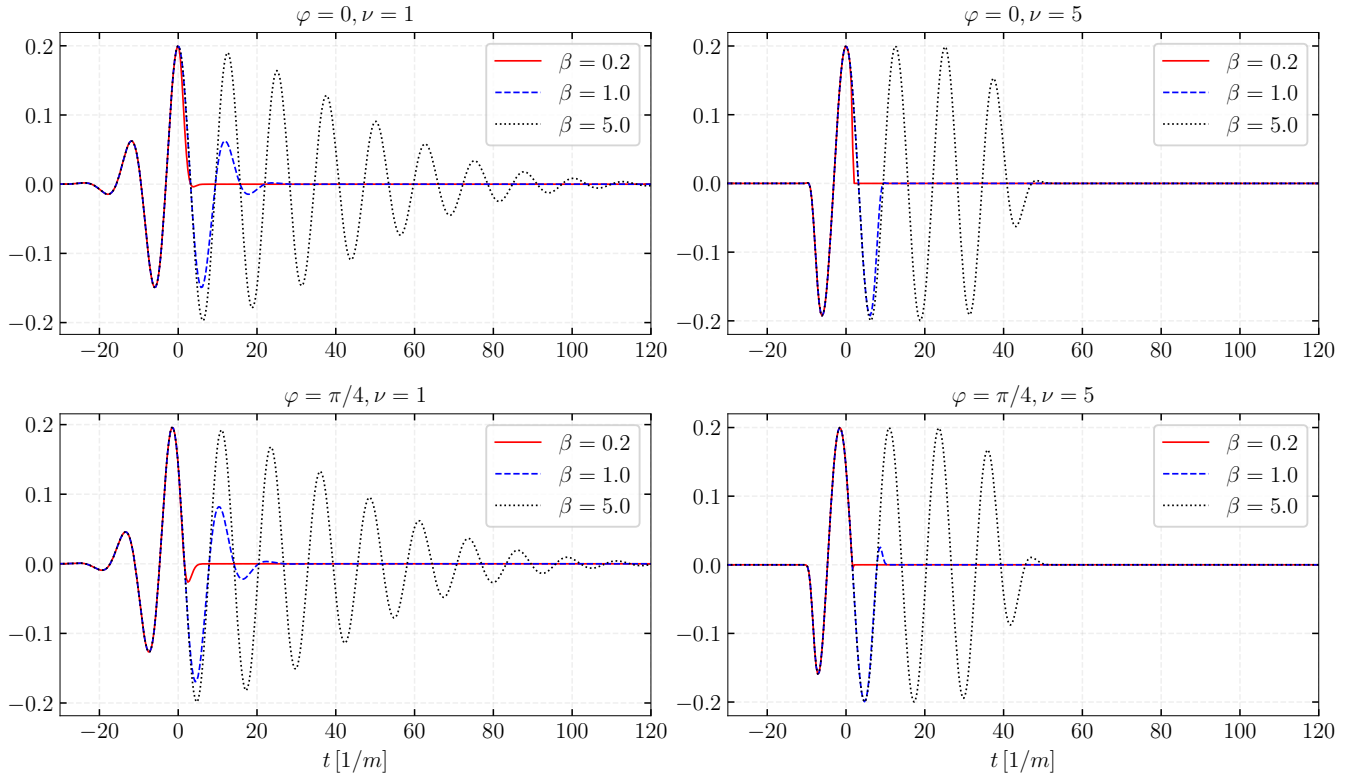


FIG. 1: Electric field with a Gaussian envelope for several combinations of  $\beta$ ,  $\varphi$  and  $\nu$ .

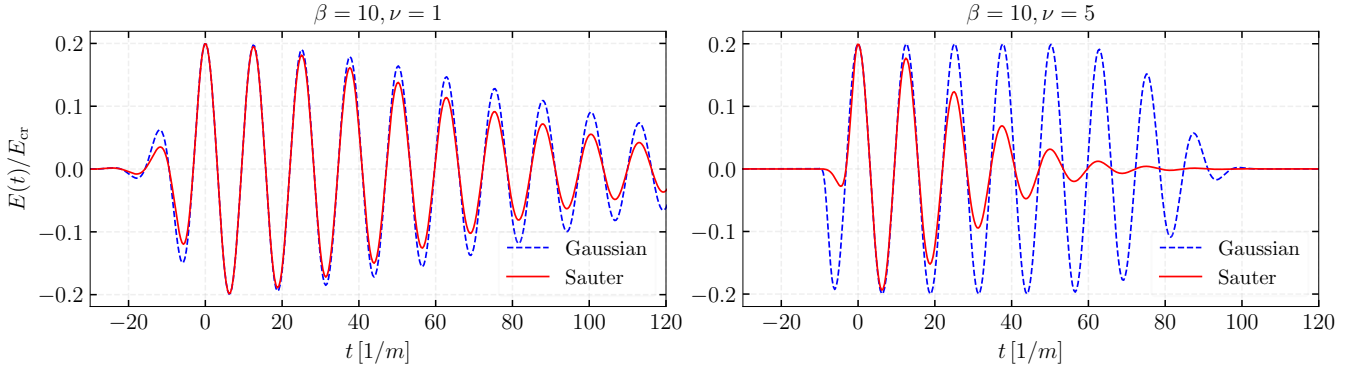


FIG. 2: Comparison of electric field profiles with Gaussian (dashed blue) and Sauter (solid red) envelopes with a large asymmetry parameter ( $\beta = 10$ ). Unlike the Gaussian case, the Sauter envelope does not become flatter as  $\nu$  is increased.

Fig. 1 shows the electric field (9) with a Gaussian envelope for several values of  $\beta$ ,  $\varphi$  and  $\nu$ . A key distinction between the field profiles is that the Gaussian and Lorentzian envelopes become increasingly flat-topped as their width  $\tau$  and the order  $\nu$  are increased, whereas the Sauter envelope does not. The reason is simple: we have defined the Sauter envelope such that the power  $2\nu$  acts on the function  $\text{sech}$  rather than its argument. Fig. 2 illustrates this behavior. Whether or not an envelope develops a flat top has important implications for the momentum distribution of the produced pairs, as we will discuss in the next section.

We now discuss the numerical values of the field parameters. For sub-critical fields ( $E_0 < E_{\text{cr}}$ ) the density of produced pairs is low enough that the induced backreaction current can be neglected [19, 35–41]. In this regime, the total electric field is essentially identical to the external electric field. Further, vacuum pair production by an external electric field can occur by two different mechanisms: a non-perturbative tunneling mechanism (the Schwinger effect) and a perturbative multiphoton absorption process. The Keldysh parameter  $\gamma = mw/(eE_0)$  distinguishes between the two regimes:  $\gamma \ll 1$  indicates the non-perturbative regime, while  $\gamma \gg 1$  indicates the

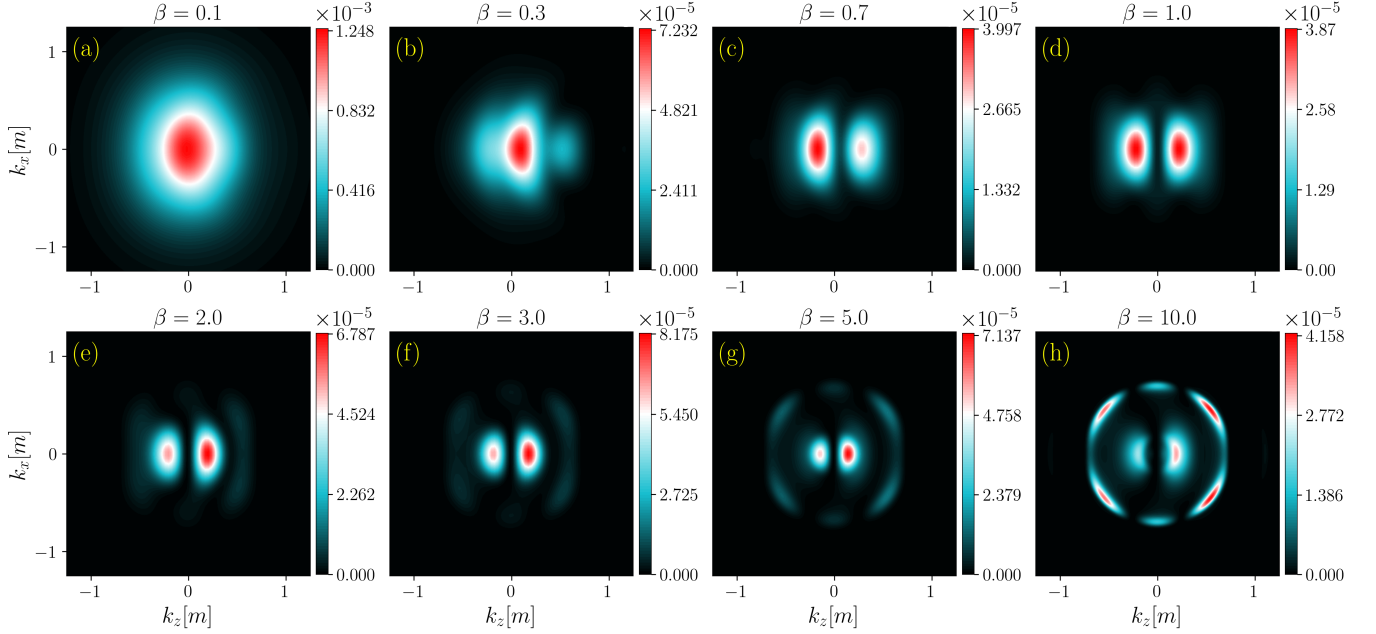


FIG. 3: Momentum distribution  $f_{\mathbf{k}}(\infty)$  with  $k_y = 0$  for a Gaussian envelope with  $\varphi = 0$  and  $\nu = 1$ .

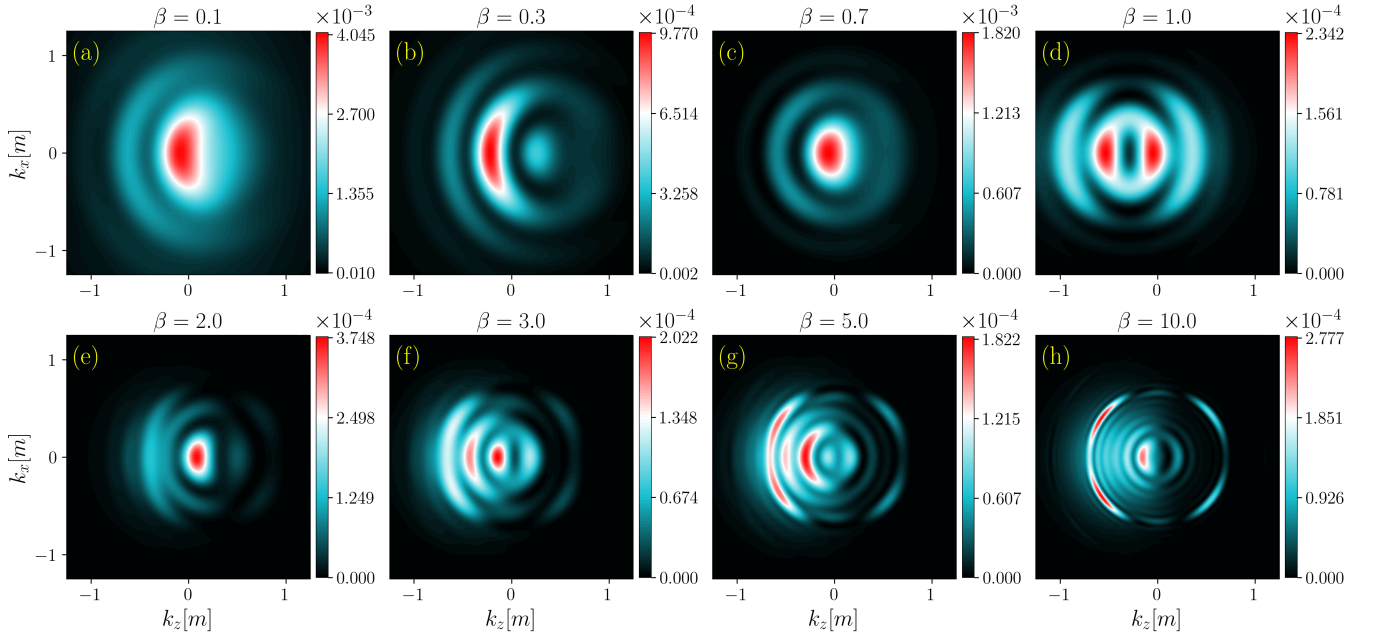


FIG. 4: Same as Fig. 3 but with  $\nu = 5$ .

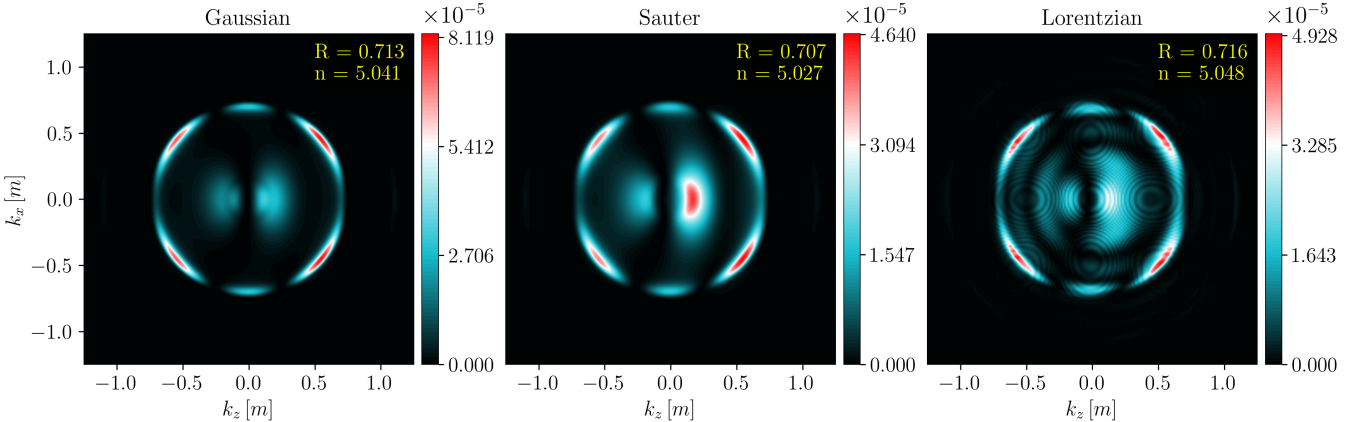
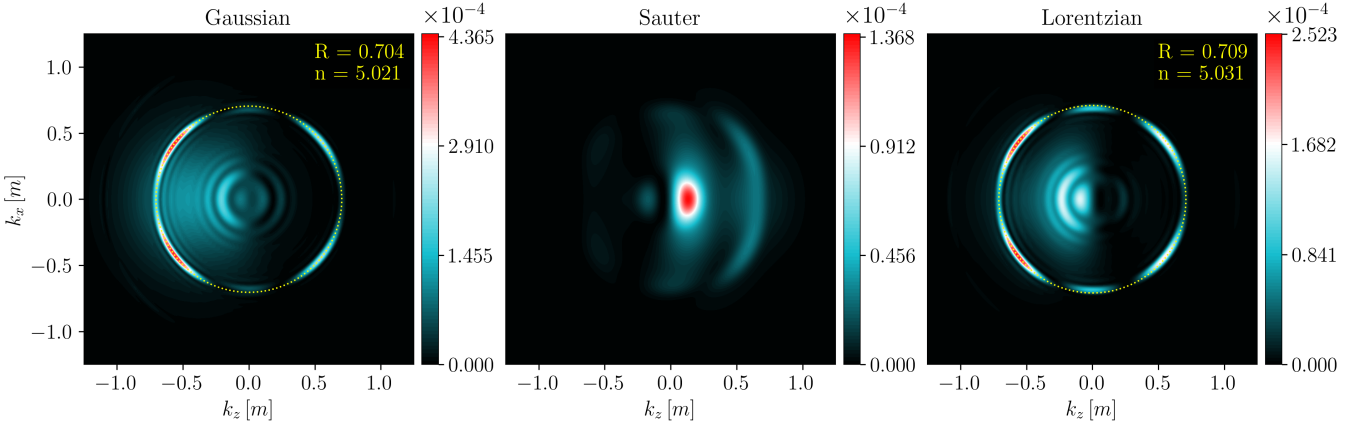
perturbative regime [42–44]. Throughout this work, we use the field parameters

$$E_0 = 0.2 E_{\text{cr}}, \quad \omega = 0.5 m, \quad \tau_1 = 8/m. \quad (13)$$

These values correspond to a subcritical field, which allows us to ignore backreaction effects. The Keldysh parameter evaluates to  $\gamma = 2.5$ , so we expect both perturbative and non-perturbative mechanisms to contribute to the pair production.

### III. MOMENTUM DISTRIBUTION

In this section we present numerical results for the asymptotic momentum distribution of the produced pairs for a range of field parameters. As mentioned above, we fix the rising pulse width at  $\tau_1 = 8/m$  and vary the falling pulse width as  $\tau_2 = \beta\tau_1$ . We also set  $k_y = 0$  whenever plotting the momentum distributions. This does not entail a loss of generality because the system



exhibits a cylindrical symmetry about the  $z$ -axis due to the fact that the electric field is linearly polarized and directed along that axis. Obviously, this cylindrical symmetry need not persist for other polarizations [16, 17]. Furthermore, by choosing the reference point of the vector potential at  $t = \infty$  in (2), the distinction between the canonical and kinetic momentum is removed in the asymptotic region.

### A. Field asymmetry and steepness effects

In Fig. 3, we show the asymptotic momentum distribution  $f_{\mathbf{k}}(\infty)$  for a Gaussian envelope with parameters  $\nu = 1$  and  $\varphi = 0$ , illustrating the effects of a compressed falling pulse (top row) and an elongated falling pulse (bottom row). The panels are ordered such that the falling pulse width increases from top-left to bottom-

right. As  $\beta$  increases, the distribution undergoes a clear qualitative and quantitative change. The peak value of the distribution falls sharply as  $\beta$  increases, up to  $\beta \approx 1$ , and then increases gradually. The large peak for  $\beta < 1$  results from the strong asymmetry and steep *switch-off* of the electric field, whereas for  $\beta > 1$  the more modest increase is driven solely by asymmetry. A detailed discussion of the effects of rapid switching on and off of strong electric backgrounds on pair production can be found in Ref. [45], where it is shown that sufficiently sharp field profiles can lead to an enhancement of pair production similar to that observed in the dynamically assisted Schwinger effect.

In Fig. 4, we again plot  $f_{\mathbf{k}}(\infty)$  for a (super-)Gaussian envelope with parameters  $\nu = 5$  and  $\varphi = 0$ . The parameter  $\nu$  controls the steepness of the electric field (i.e. the switch-on switch-off rate) and, unlike  $\beta$ , does not alter the electric field's symmetry. Increasing  $\beta$  at  $\nu = 5$

produces qualitative trends similar to those observed for  $\nu = 1$ . However, for any fixed  $\beta$ , the distribution function now exhibits more peaks, and significantly taller ones, than in the  $\nu = 1$  case. This behavior is explained by the fact that increasing  $\nu$  enhances the effective time during which the field remains near its maximum value. Another reason is the appearance of higher-frequency components in the Fourier spectrum of the electric field, which we discuss in greater detail in Sec. IV. Thus, our results clearly demonstrate that steepness has a greater effect on the particle production rate than asymmetry does.

We observe that the momentum distribution for the  $\beta = 1, \nu = 1$  field (Fig. 3 (d)) exhibits an approximate  $k_z$ -reflection symmetry ( $k_z \rightarrow -k_z$ ) while that for the  $\beta = 1, \nu = 5$  field (Fig. 4 (d)) does not, despite both distributions corresponding to an electric field even in time. The net impulse  $-e \int_{-\infty}^{\infty} E(t) dt$  carried by the  $\beta = 1, \nu = 1$  field is negligible, allowing the vector potential to remain effectively odd and nearly preserving the symmetry. For the  $\beta = 1, \nu = 5$  case the field profile is narrower, such that essentially only a few oscillation cycles fit in the pulse. Consequently, the cosine is no longer averaged out, and the net impulse has a non-negligible value resulting in the broken symmetry.

We also observe that, for a fixed  $\nu$ , the number of peaks increases with  $\beta$ . This behavior is actually not universal and strongly depends on the field parameters. In Ref. [14] the number of peaks decreases as  $\beta$  increases, whereas in Ref. [34] it remains essentially constant as  $\beta$  changes.

For envelopes that become effectively flat-topped at large  $\beta$ , the outer peaks coalesce into ring-like interference structures. In fact, at large enough  $\beta$  the ring-like structures can completely dominate the distribution; the central peaks only dominate if  $\beta$  is small or if the envelope is not flat-topped. The rings also become more prominent as  $\nu$  increases. These rings correspond to multiphoton absorption and emerge when the electric field features a long falling pulse [16]. Their radius follows from energy conservation:

$$|\mathbf{k}| = \sqrt{\left(\frac{n\omega}{2}\right)^2 - m_*^2}, \quad (14)$$

where  $m_* = m \sqrt{1 + \frac{e^2 E_0^2}{2m^2 \omega^2}}$  is the effective mass and  $n$  denotes the number of absorbed photons [24]. Physically, this expression means that the absorption of  $n$  photons of frequency  $\omega$ , shared between the electron and the positron, produces a characteristic excess momentum  $\mathbf{k}$ . Although (14) is strictly valid only for plane-wave fields, a faint partially formed ring is already visible at  $\beta = 3$  in Fig. 3 (f). The number of photons associated with the smallest ring follows directly from (14):

$$n_{\min} = \text{ceil}\left(\frac{2m_*}{\omega}\right). \quad (15)$$

For the parameters used in this work ( $E_0 = 0.2E_{\text{cr}}$ ,  $\omega = 0.5 \text{ m}$ ), we obtain  $n_{\min} = 5$ . In Fig. 5 (for  $\nu = 5$ ) and in

Fig. 6 (for  $\nu = 1$ ) we plot  $f_{\mathbf{k}}(\infty)$  for a very long falling pulse ( $\beta = 15$ ). Multiphoton rings appear in all cases except for the  $\nu = 5$  Sauter envelope. As discussed above, the long or flat-topped falling pulse at  $\beta = 15$  enhances the multiphoton contribution. This mechanism is absent from the Sauter envelope with  $\nu = 5$ , which switches-off rapidly due to the large  $\nu = 5$  and therefore does not produce rings. Fig. 2 compares the Gaussian and Sauter envelopes with  $\nu = 1$  and  $\nu = 5$ . Also see Refs. [46–48] for pair production by super-Gaussian envelopes.

## B. Carrier-envelope phase effects

The carrier-envelope phase (CEP)  $\varphi$  has a pronounced impact on the structure of the electric field profile, influencing both the positions of the extrema and the symmetry of the profile about  $t = 0$  (see Fig. 1). It also determines how many oscillations of the carrier wave fit within the pulse envelope. Consequently, CEP plays an especially significant role for ultrashort pulses, where only a few carrier cycles lie within the envelope [25, 46]. See also Ref. [49] for a discussion of relative-phase effects in dynamically assisted fields.

Fig. 7 (for  $\nu = 1$ ) and Fig. 8 (for  $\nu = 5$ ) show the momentum distributions for a Gaussian envelope for various combinations of CEP ( $\varphi$ ) and  $\beta$ . We find that the sensitivity of the momentum distribution and its peak to CEP, both in terms of its position and height, decreases as the width of the falling pulse increases. For very elongated falling pulses the effect is negligible, whereas for very short falling pulses a change in CEP can change the momentum distribution at and around the peak by an entire order of magnitude.

Further comparison between Fig. 3 (d) and Fig. 7 (c, g) shows that CEP alone can break the momentum-inversion symmetry. In distributions that already lack the inversion symmetry, CEP may exaggerate the asymmetry. In addition, the number of peaks in the momentum distribution is strongly influenced by CEP: Fig. 3 (b) exhibits a single dominant peak whereas for a nonzero CEP the distribution in Fig. 7 (b) splits into two distinct peaks. See Refs. [50, 51] for the effects of CEP on pair production in spatially inhomogeneous electric fields.

## C. Semiclassical analysis

To interpret the features in the momentum distributions and number densities shown in Secs. III and IV, we employ a semiclassical turning point (saddle point) analysis. It is based on the fact that vacuum decay in a spatially homogeneous time-dependent electric field can be recast as a one dimensional over-the-barrier quantum mechanical scattering problem. The pair-creation amplitude is controlled by the classical action evaluated on trajectories in the complex-time plane where the longitudinal momentum vanishes [10, 43, 52–54].

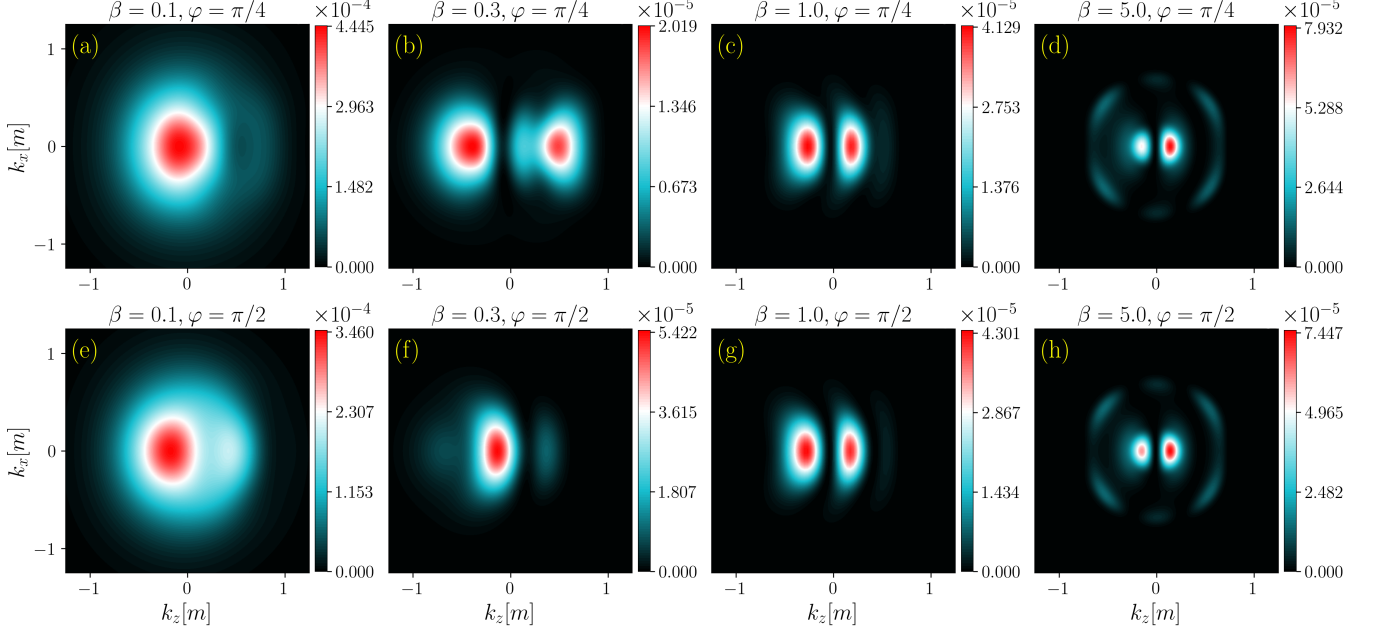


FIG. 7: Momentum distribution  $f_{\mathbf{k}}(\infty)$  with  $k_y = 0$  for Gaussian envelope with non-zero  $\varphi$  and  $\nu = 1$ . Compare with Fig. 3.

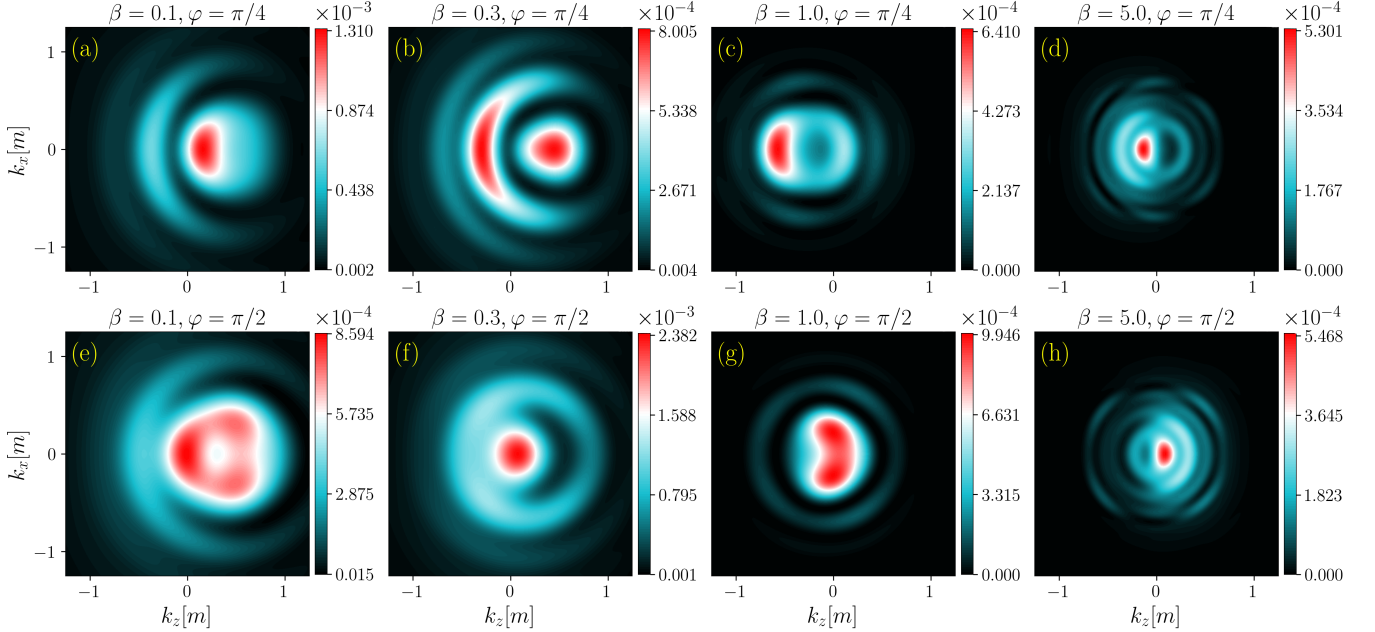


FIG. 8: Same as Fig. 7 but with  $\nu = 5$ . Compare with Fig. 4

The turning points  $t_i$  of the equivalent scattering potential are defined by  $\Omega_{\mathbf{k}}(t_i) = 0$ . By applying the standard WKB treatment, the asymptotic momentum distribution is found to be [32, 52, 55]

$$f_{\mathbf{k}}(\infty) \approx \sum_i e^{-2K_{\mathbf{k}}^i} + \sum_{i \neq j} 2 \cos(2\theta_{\mathbf{k}}^{ij})(-1)^{i-j} e^{-K_{\mathbf{k}}^i - K_{\mathbf{k}}^j} \quad (16)$$

where

$$K_{\mathbf{k}}^i = \left| \int_{t_i^*}^{t_i} \Omega_{\mathbf{k}}(t) dt \right|, \quad \theta_{\mathbf{k}}^{ij} = \left| \int_{\text{Re}(t_i)}^{\text{Re}(t_j)} \Omega_{\mathbf{k}}(t) dt \right|. \quad (17)$$

This equation is accurate provided  $f_{\mathbf{k}}(\infty) \ll 1$ .

Each turning point  $t_i$  contributes separately an exponentially suppressed term  $e^{-2K_{\mathbf{k}}^i}$ . Turning points farther from the real axis have larger imaginary parts, yielding larger  $K_{\mathbf{k}}^i$  and thus weaker contributions. Interference

between pairs of turning points is contained in the second term in (16) and is appreciable only when the involved turning points have comparable values of  $K_{\mathbf{k}}^i$ ; otherwise the cross term is exponentially suppressed. A practical guideline is thus: turning points closest to the real axis tend to dominate the distribution, and interference is strongest between turning point pairs with similar distances from the real axis. Of course, depending on the structure of  $A(t)$ , other pairs of turning points can also interfere strongly.

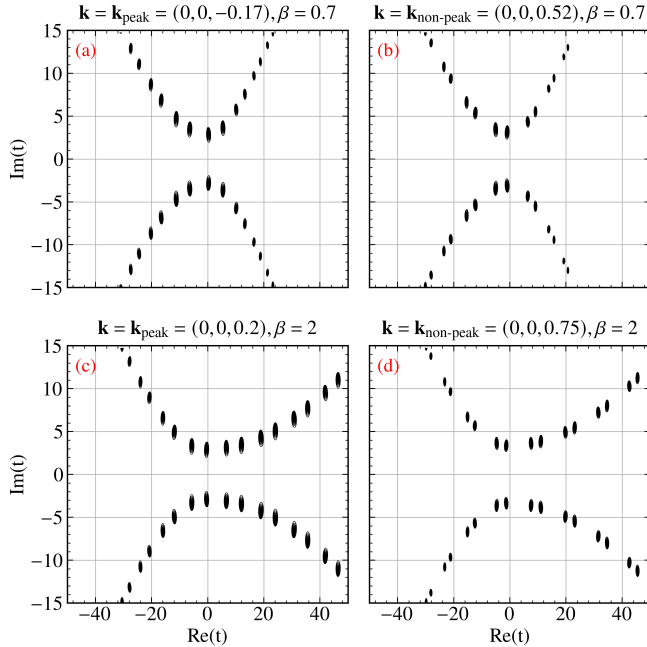


FIG. 9: Contour plots of  $|\Omega_{\mathbf{k}}(t)|^2$  in the complex- $t$  plane showing the locations of the turning points where  $\Omega_{\mathbf{k}}(t) = 0$ . These plots are for  $\nu = 1$  and  $\varphi = 0$ . The figure illustrates the change in the turning points as the momentum is changed from the peak value (left panels) to a non-peak value (right panels) while keeping  $\beta$  fixed.

In this work, we present, for the first time, the turning point structure for a nonanalytic field of the form (9). To enable a well-defined turning point analysis, we regularize the non-analyticity at  $t = 0$  by replacing the Heaviside step function with a sigmoid function. The details of this regularization and the numerical procedure used to identify the turning points are given in Appx. B. In this section, we restrict our discussion to the results obtained for the Gaussian envelope.

In Fig. 9, panels (a) and (c) show the turning point structure at momenta corresponding to the peaks in Fig. 3 (c) and (d) respectively. Panels (b) and (d) in Fig. 9 show turning points at nearby momenta where the momentum distribution has a smaller value. In all cases the turning points arrange themselves in an infinitely tall hourglass structure symmetric about the real axis. The key difference lies in the proximity of turning points to the real axis: the momenta at the peaks correspond to

turning points closer to the real axis as compared to those off the peaks. This aligns with the insight from (16) and explains the larger values of the distribution at the peaks, and also the relatively weak interference in Figs. 3 (c) and (d) as most turning points beyond the first few are strongly suppressed.

To illustrate how the asymmetry parameter  $\beta$  modifies the interference structure, Fig. 10 shows turning points at peak momenta for several values of  $\beta$ . For small  $\beta$ , the hourglass shape is narrow and well-separated from the real axis. As  $\beta$  increases, the hourglass broadens and the turning points move closer to the real axis. Consequently, a larger number of turning points contribute significantly to the second term in (16), leading to a pronounced strengthening of the interference patterns, as shown in Fig. 3.

Fig. 11 illustrates how the super-Gaussian order  $\nu$  affects the turning point structure. Panels (a) and (b) of Fig. 11 correspond to the peaks of Figs. 7 (h) and 8 (h), respectively. Increasing  $\nu$  brings more pairs of turning points to similar distances from the real axis, thereby raising the peak and contributing to a stronger interference pattern. A corresponding trend appears in panels (c) and (d) of Fig. 11, which explain the stronger interference and the larger peak value in Fig. 4 (h) compared to Fig. 3 (h).

#### IV. NUMBER DENSITY

In this section, we focus on the number density in asymmetric (super-)Gaussian electric fields. See Fig. 12 for plots of the number density as a function of the CEP  $\varphi$ , for several values of the asymmetry parameter  $\beta$  and the super-Gaussian order  $\nu$ .

It is clear from the plots that field profiles with shorter falling pulses (large  $\nu$  or small  $\beta$ ) consistently yield higher particle densities. The effect of steepness, which is controlled by  $\nu$  and  $\beta$  independently, outsizes that of asymmetry, which is controlled only by  $\beta$ . This aligns with the discussion in Sec. III. Increasing  $\nu$  increases the higher frequency components in the Fourier spectrum of the electric field, which leads to a significant enhancement in pair production due to the fact that higher frequency components can introduce multiphoton channels thereby enhancing pair production beyond the purely tunneling regime [45]. See Appx. A for a discussion on the Fourier analysis of the electric field, and Fig. 13 for Fourier spectra of the electric field for various values of  $\beta$  and  $\nu$ . On decreasing  $\beta$ , the two dominant peaks in the Fourier spectra become shorter and wider; thus  $\beta$  also has a steepness effect, but less pronounced than that of  $\nu$ . As a result, we see an overall decrease in the number density with increase in  $\beta$  values.

Fig. 12 also shows that the sensitivity of the number density to the CEP  $\varphi$  is greatly affected by  $\nu$  and  $\beta$ . At  $\nu = 1$  the distribution is barely sensitive to CEP, unless  $\beta$  is very small, whereas at  $\nu = 5$  and small  $\beta$  a change in

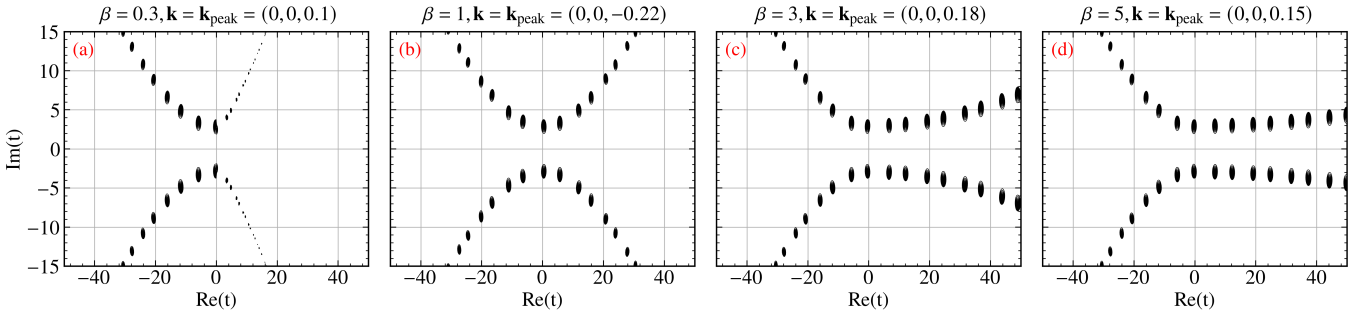


FIG. 10: Contour plots of  $|\Omega_{\mathbf{k}}(t)|^2$  in the complex- $t$  plane showing the locations of the turning points where  $\Omega_{\mathbf{k}}(t) = 0$ . These plots are for  $\nu = 1$  and  $\varphi = 0$  at peak momentum values for various  $\beta$ .

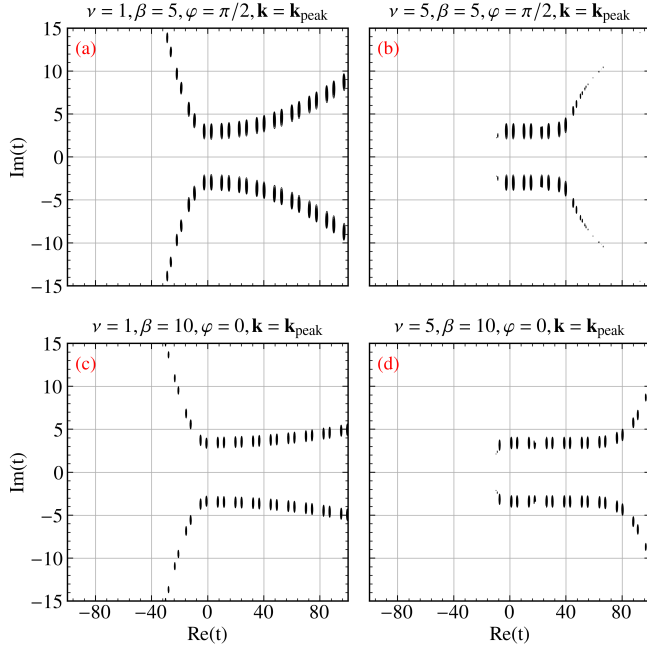


FIG. 11: Contour plots of  $|\Omega_{\mathbf{k}}(t)|^2$  in the complex- $t$  plane showing the locations of the turning points where  $\Omega_{\mathbf{k}}(t) = 0$ . The figure illustrates the change in the turning points as the field profile changes from Gaussian  $\nu = 1$  (left panels) to super-Gaussian  $\nu = 5$  (right panels). From upper left to lower right,  $\mathbf{k}_{\text{peak}}$  are  $(0, 0, 0.14)$ ,  $(0, 0, 0.8)$ ,  $(0.45, 0, 0.55)$ ,  $(0.35, 0, -0.6)$ .

CEP can cause the total yield to increase by two to three orders of magnitude. This behavior can be explained by the fact that CEP controls the number of oscillations in the envelope much more strongly when the field has a short falling pulse (large  $\nu$  or small  $\beta$ ). An elongated falling pulse does not preserve the subcycle structure and the long pulse width averages out the effect of CEP. A similar observation was made in Ref. [46] where the authors find the number density to have a higher sensitivity to  $\varphi$  in the subcycle pulse case as compared to the supercycle case.

## V. CONCLUSION AND DISCUSSION

In this work, we have investigated the combined effects of carrier envelope phase (CEP) and laser pulse shape on pair production and momentum distribution in asymmetric electric fields with bell-shaped envelopes. We used three different bell-shaped envelopes (Gaussian, Sauter and Lorentzian) in order to be able to derive general results which do not depend on the exact details of the envelope. In particular, the Sauter envelope was defined to never be flat-topped in any limit. We used separate parameters to control the steepness and the asymmetry, so as to be able to differentiate their effects. The momentum distribution and the total density of the created particles were obtained by numerically solving the quantum Vlasov equation (QVE).

The overall effect of asymmetry is to increase the peak values in the momentum distribution and, thereby, the number density. For asymmetric flat-topped field profiles with elongated falling pulses, we identified ring-shaped interference patterns corresponding to pair creation by multiphoton absorption. The radii of the rings were found numerically, and they match very well with theoretical predictions based on simple energy conservation despite the fact that the field profiles are not plane waves. If the field profile is not flat-topped, then there are no significant multiphoton interference patterns.

Decreasing the width of a field profile, which may be symmetric or not, increases the short-edge effect and enhances particle production. The short-edge effect is easily explained by the appearance of higher frequency peaks in the Fourier spectrum of the electric field. This enhancement is significantly stronger than that achieved by increasing the asymmetry in the field profile. Therefore, it is better to shorten the falling pulse in order to increase the pair production.

We also found that CEP is a critical control parameter for short pulses as the momentum distribution and number density are extremely sensitive to CEP for short pulses. The effect of CEP diminishes as the pulse width increases. We found the number density to be the largest when the field profile was very short and had a non-zero CEP; however, this statement is sensitive to the field pa-

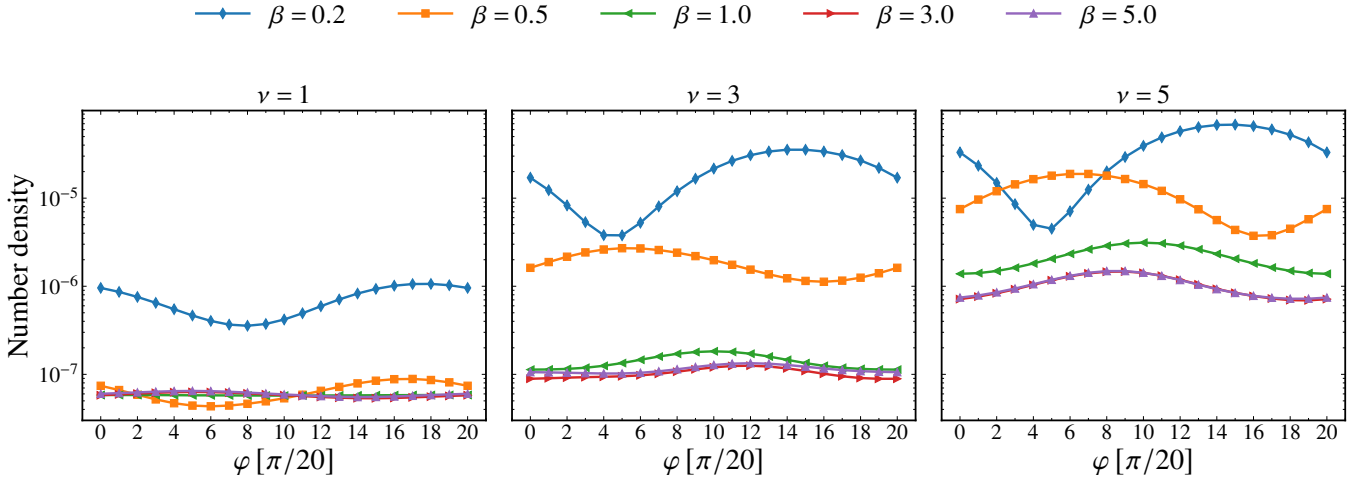


FIG. 12: Number density (in units of  $m^{-3}$ ) as a function of the CEP  $\varphi$  in (super-)Gaussian asymmetric electric fields.

rameters that were kept fixed in this study (such as the electric field amplitude and carrier frequency). We have explained the interference patterns in the momentum distribution by analyzing the turning points of the single-particle dispersion relation. The turning points form an hourglass structure in the complex-time plane. If the hourglass is broader for some parameter values, then the turning points are closer to the real axis. This causes the interference effects to become stronger and the fringes more numerous.

These findings highlight that careful optimization of pulse duration, envelope shape, and CEP offers a viable way to maximize pair production.

### Appendix A: Fourier Analysis

In Fig. 13, we plot the Fourier transform of the electric field

$$\tilde{E}(\omega') = \int_{-\infty}^{\infty} E(t) e^{i\omega' t} dt. \quad (\text{A1})$$

as a function of the frequency  $\omega'$  for (super-)Gaussian envelopes for various values of the asymmetry parameter  $\beta$  and super-Gaussian order  $\nu$ . In each case, there are two dominant symmetric peaks. As  $\nu$  increases, the envelope becomes steeper, leading to the appearance of higher frequency peaks in the Fourier spectra. These contributions, while having a relatively small weight, are important as they correspond to multiphoton channels that can substantially enhance the pair production. Consequently, increasing  $\nu$  strengthens the high-frequency tail in the spectrum, which in turn boosts the overall number density. Also note that the peak is broader for smaller values of the pulse asymmetry parameter  $\beta$ . This explains the enhancement in particle production in the case of smaller values of  $\beta$  (cf. Sec. IV).

### Appendix B: Numerical identification of turning points

The electric field (9) consists of two envelopes that switch at  $t = 0$  by means of two Heaviside step functions.

As the Heaviside step function is not differentiable at  $t = 0$ , analytic continuation of the profile to complex- $t$  plane is not possible directly. We bypass this problem by replacing the Heaviside step function with a smooth sigmoid function as

$$\Theta(t) \rightarrow \Theta_{\epsilon}(t) = \frac{1}{2} \left[ 1 + \tanh \left( \frac{t}{\epsilon} \right) \right], \quad \epsilon > 0. \quad (\text{B1})$$

The parameter  $\epsilon$  acts as a smoothing parameter; it controls the steepness of  $\Theta_{\epsilon}(t)$  around  $t = 0$ . As this regularization is based on the identity  $\lim_{\epsilon \rightarrow 0} \Theta_{\epsilon}(t) = \Theta(t)$ , we fix  $\epsilon = 0.05$  throughout this work. The maximum relative error introduced in the electric field by this small but non-zero  $\epsilon$  is 0.02% for  $\beta = 0.1$  and  $\nu = 1$  and it sharply decreases as  $\beta$  or  $\nu$  are increased. For example, at  $\beta = 15$  and  $\nu = 5$  the maximum relative error is  $10^{-14}\%$ . The resulting regularized electric field  $E_{\epsilon}(t)$  is analytic in  $t$ , and therefore admits a well-defined analytic vector potential. Analyticity ensures that the vector potential depends only on the reference point and not the integration path in the complex- $t$  plane.

To locate the turning points of  $\Omega_{\mathbf{k}}(t)$  in the complex- $t$  plane, we use an indirect contour-based method developed in Refs. [30, 52, 56]. Rather than solving  $\Omega_{\mathbf{k}}(t) = 0$  directly, turning points are identified by plotting logarithmically spaced contours (on a uniformly spaced grid) defined by

$$|\Omega_{\mathbf{k}}(t)|^2 = \delta, \quad (\text{B2})$$

with  $\delta$  ranging from  $10^{-10}$  to  $10^{-1}$ . The turning points manifest themselves as islands in these contour plots, as families of closed contours, parameterized by  $\delta$ , converge towards the turning points.

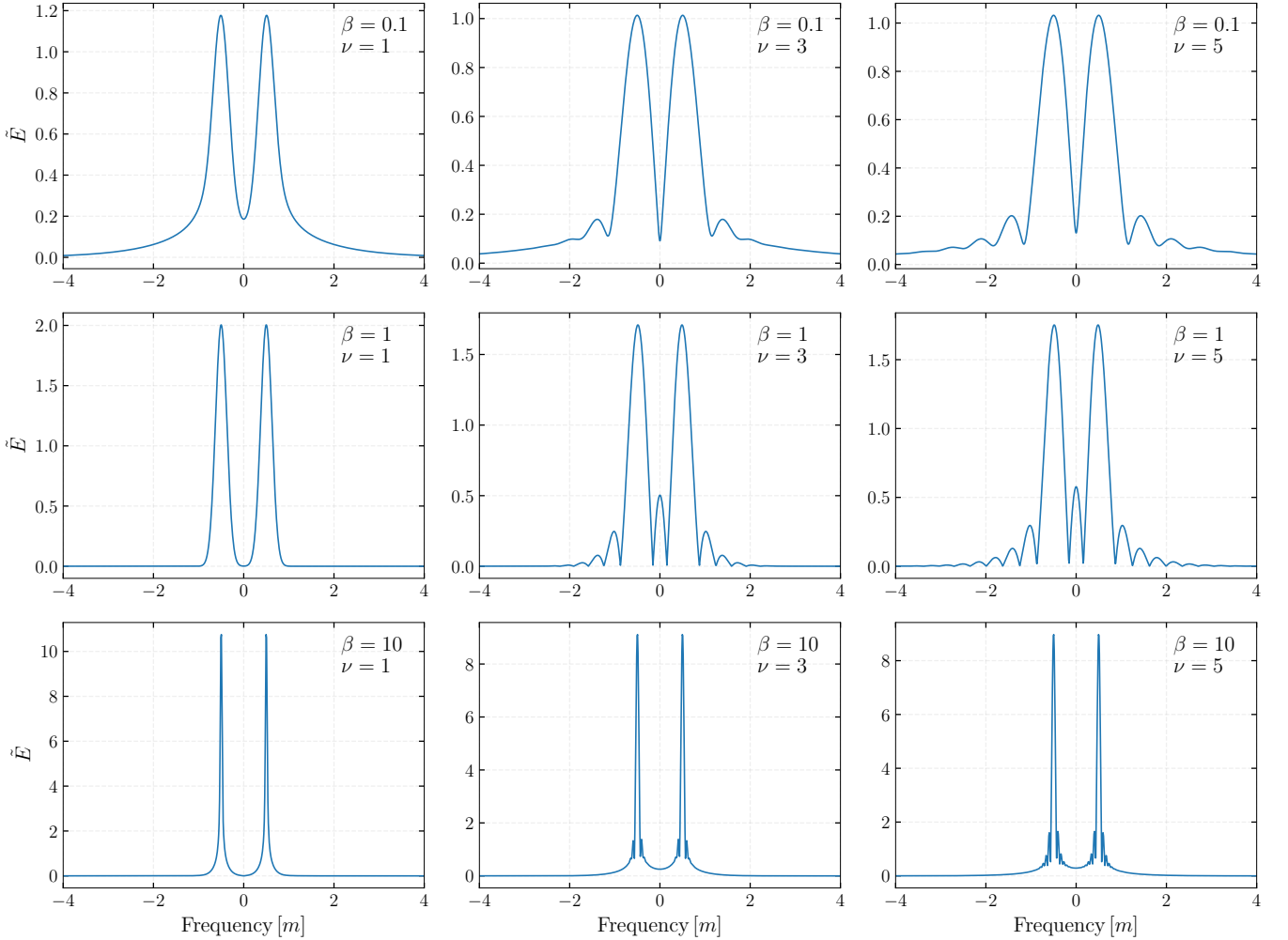


FIG. 13: Fourier transform  $\tilde{E}$  of the asymmetric (super-)Gaussian electric fields with  $\varphi = 0$ . The two tallest peaks are located at  $\omega' = \pm\omega$ . Other peaks appear as  $\nu$  is increased. The field parameters are the same as those used throughout this work:  $E_0 = 0.2E_{\text{cr}}$ ,  $\omega = 0.5m$  and  $\tau_1 = 8/m$ .

---

[1] P. A. M. Dirac, The quantum theory of the electron, Proceedings of the Royal Society of London. Series A, Containing Papers of a Mathematical and Physical Character **117**, 610 (1928).

[2] F. Sauter, On the behavior of an electron in a homogeneous electric field in dirac's relativistic theory, Z. Phys **69**, 742 (1931).

[3] J. Schwinger, On gauge invariance and vacuum polarization, Physical Review **82**, 664 (1951).

[4] D. Strickland and G. Mourou, Compression of amplified chirped optical pulses, Optics communications **55**, 447 (1985).

[5] J. W. Yoon, Y. G. Kim, I. W. Choi, J. H. Sung, H. W. Lee, S. K. Lee, and C. H. Nam, Realization of laser intensity over 1023 w/cm<sup>2</sup>, Optica **8**, 630 (2021).

[6] <https://www.eli-laser.eu/>.

[7] <https://www.xfel.eu/>.

[8] A. Ringwald, Pair production from vacuum at the focus of an x-ray free electron laser, Physics Letters B **510**, 107 (2001).

[9] E. Khazanov, A. Shaykin, I. Kostyukov, V. Ginzburg, I. Mukhin, I. Yakovlev, A. Soloviev, I. Kuznetsov, S. Mironov, A. Korzhimanov, *et al.*, exawatt center for extreme light studies, High Power Laser Science and Engineering **11**, e78 (2023).

[10] V. Popov, Pair production in a variable external field (quasiclassical approximation), Soviet Journal of Experimental and Theoretical Physics **34**, 709 (1972).

[11] G. Dunne *et al.*, From fields to strings: circumnavigating theoretical physics, Heisenberg–Euler Effective Lagrangians: Basics and Extensions **1**, 445 (2005).

[12] G. V. Dunne and C. Schubert, Worldline instantons and pair production in inhomogenous fields, Physical Review D-Particles, Fields, Gravitation, and Cosmology **72**, 105004 (2005).

[13] O. Olugh, Z.-L. Li, B.-S. Xie, and R. Alkofer, Pair pro-

duction in differently polarized electric fields with frequency chirps, *Physical Review D* **99**, 036003 (2019).

[14] N.-Z. Chen, O. Amat, L.-N. Hu, H.-H. Fan, and B.-S. Xie, Asymmetric pulse effects on pair production in chirped electric fields, *Physical Review D* **109**, 076015 (2024).

[15] F. Hebenstreit, *Schwinger effect in inhomogeneous electric fields*, Ph.D. thesis, University of Graz (2011).

[16] A. Blinne, *Electron positron pair production in strong electric fields*, Ph.D. thesis, University of Jena (2016).

[17] Z. Li, D. Lu, and B. Xie, Effects of electric field polarizations on pair production, *Physical Review D* **92**, 085001 (2015).

[18] Y. Kluger, E. Mottola, and J. M. Eisenberg, Quantum vlasov equation and its markov limit, *Physical Review D* **58**, 125015 (1998).

[19] R. Alkofer, M. Hecht, C. D. Roberts, S. Schmidt, and D. Vinnik, Pair creation and an x-ray free electron laser, *Physical Review Letters* **87**, 193902 (2001).

[20] D. Blaschke, A. Prozorkevich, C. Roberts, S. Schmidt, and S. Smolyansky, Pair production and optical lasers, *Physical review letters* **96**, 140402 (2006).

[21] M. Orthaber, F. Hebenstreit, and R. Alkofer, Momentum spectra for dynamically assisted schwinger pair production, *Physics Letters B* **698**, 80 (2011).

[22] G. R. Mocken, M. Ruf, C. Müller, and C. H. Keitel, Non-perturbative multiphoton electron-positron-pair creation in laser fields, *Physical Review A—Atomic, Molecular, and Optical Physics* **81**, 022122 (2010).

[23] M. Ruf, G. R. Mocken, C. Müller, K. Z. Hatsagortsyan, and C. H. Keitel, Pair production in laser fields oscillating in space and time, *Physical review letters* **102**, 080402 (2009).

[24] C. Kohlfürst, H. Gies, and R. Alkofer, Effective mass signatures in multiphoton pair production, *Physical Review Letters* **112**, 050402 (2014).

[25] F. Hebenstreit, R. Alkofer, G. V. Dunne, and H. Gies, Momentum signatures for schwinger pair production in short laser pulses with a subcycle structure, *Physical review letters* **102**, 150404 (2009).

[26] R. Schützhold, H. Gies, and G. Dunne, Dynamically assisted schwinger mechanism, *Physical review letters* **101**, 130404 (2008).

[27] A. Nuriman, B.-S. Xie, Z.-L. Li, and D. Sayipjamal, Enhanced electron-positron pair creation by dynamically assisted combinational fields, *Physics Letters B* **717**, 465 (2012).

[28] C. Fey and R. Schützhold, Momentum dependence in the dynamically assisted sauter-schwinger effect, *Physical Review D—Particles, Fields, Gravitation, and Cosmology* **85**, 025004 (2012).

[29] L.-J. Li, M. Mohamedsedik, and B.-S. Xie, Enhanced dynamically assisted pair production in spatial inhomogeneous electric fields with the frequency chirping, *Physical Review D* **104**, 036015 (2021).

[30] C. K. Dumlu, Schwinger vacuum pair production in chirped laser pulses, *Physical Review D—Particles, Fields, Gravitation, and Cosmology* **82**, 045007 (2010).

[31] J. Min *et al.*, *Chin. Phys. B* **22**, 100307 (2013).

[32] C. Gong, Z. Li, B. Xie, and Y. Li, Electron-positron pair production in frequency modulated laser fields, *Physical Review D* **101**, 016008 (2020).

[33] O. Oluk, B.-S. Xie, M. A. Bake, and S. Dulat, Electron-positron pair production in a strong asymmetric laser electric field, *Frontiers of Physics* **9**, 157 (2014).

[34] O. Olugh, Z.-L. Li, and B.-S. Xie, Asymmetric pulse effects on pair production in polarized electric fields, *High Power Laser Science and Engineering* **8**, e38 (2020).

[35] J. C. Bloch, V. Mizerny, A. Prozorkevich, C. D. Roberts, S. Schmidt, S. Smolyansky, and D. Vinnik, Pair creation: Back reactions and damping, *Physical Review D* **60**, 116011 (1999).

[36] N. Tanji, Dynamical view of pair creation in uniform electric and magnetic fields, *Annals of Physics* **324**, 1691 (2009).

[37] S. Smolyansky, V. Mizerny, D. Vinnik, A. Prozorkevich, and V. Toneev, The non-equilibrium distribution function of particles and anti-particles created in strong fields, in *Progress in Nonequilibrium Green's Functions* (World Scientific, 2000) pp. 375–382.

[38] D. Vinnik, A. Prozorkevich, S. Smolyansky, V. Toneev, M. Hecht, C. D. Roberts, and S. Schmidt, Plasma production and thermalisation in a strong field, *The European Physical Journal C-Particles and Fields* **22**, 341 (2001).

[39] C. Roberts, S. Schmidt, and D. Vinnik, Quantum effects with an x-ray free-electron laser, *Physical review letters* **89**, 153901 (2002).

[40] M. Prakapenia and G. Vereshchagin, Pauli blocking effects on pair creation in strong electric field, *Physical Review D* **108**, 013002 (2023).

[41] R. Jiang, C. Gong, Z. Li, and Y. Li, Backreaction effect and plasma oscillation in pair production for rapidly oscillating electric fields, *Physical Review D* **108**, 076015 (2023).

[42] L. Keldysh, Ionization in the field of a strong electromagnetic wave, *Sov. Phys. JETP* **20**, 1307 (1965).

[43] E. Brézin and C. Itzykson, Pair production in vacuum by an alternating field, *Physical Review D* **2**, 1191 (1970).

[44] V. S. Popov, Tunnel and multiphoton ionization of atoms and ions in a strong laser field (keldysh theory), *Phys. Usp.* **47**, 855 (2004).

[45] I. Aleksandrov, D. Sevostyanov, and V. Shabaev, Schwinger particle production: rapid switch off of the external field versus dynamical assistance, *Physical Review D* **111**, 016010 (2025).

[46] N. Abdukerim, Z.-L. Li, and B.-S. Xie, Effects of laser pulse shape and carrier envelope phase on pair production, *Physics Letters B* **726**, 820 (2013).

[47] A. Otto, H. Oppitz, and B. Kämpfer, Assisted vacuum decay by time-dependent electric fields, *The European Physical Journal A* **54**, 23 (2018).

[48] A. D. Panferov, S. A. Smolyansky, A. Otto, B. Kämpfer, D. B. Blaschke, and L. Juchnowski, Assisted dynamical schwinger effect: pair production in a pulsed bifrequent field, *The European Physical Journal D* **70**, 56 (2016).

[49] J. Bras *et al.*, (2025), [arXiv:2505.24488 \[hep-ph\]](https://arxiv.org/abs/2505.24488).

[50] M. Mohamedsedik, L.-J. Li, L. Wang, O. Amat, L.-N. Hu, and B. Xie, Phase effect on and symmetry of pair production in inhomogeneous electric fields with chirping, *The European Physical Journal Plus* **138**, 316 (2023).

[51] M. Mohamedsedik, L.-J. Li, and B. Xie, Schwinger pair production in inhomogeneous electric fields with symmetrical frequency chirp, *Physical Review D* **104**, 016009 (2021).

[52] C. K. Dumlu and G. V. Dunne, Interference effects in schwinger vacuum pair production for time-dependent laser pulses, *Physical Review D—Particles, Fields, Gravitation, and Cosmology* **83**, 065028 (2011).

- [53] H. Taya, T. Fujimori, T. Misumi, M. Nitta, and N. Sakai, Exact wkb analysis of the vacuum pair production by time-dependent electric fields, *Journal of High Energy Physics* **2021**, 1 (2021).
- [54] E. Akkermans and G. V. Dunne, Ramsey fringes and time-domain multiple-slit interference from vacuum, *Physical Review Letters* **108**, 030401 (2012).
- [55] Z.-L. Li, D. Lu, and B.-S. Xie, Multiple-slit interference effect in the time domain for boson pair production, *Physical Review D* **89**, 067701 (2014).
- [56] C. K. Dumlou and G. V. Dunne, Complex worldline instantons and quantum interference in vacuum pair production, *Physical Review D—Particles, Fields, Gravitation, and Cosmology* **84**, 125023 (2011).